

Equations and Tables: See Appendix A: Galley Proof Sample of a JCTN publication.

Manuscript Title:

Polarity Reversion of the Operation Mode of HfO₂-Based Resistive Random Access Memory Devices by Inserting Hf Metal Layer

Name Format: FirstName MiddleName FamilyName

Ching-Shiang Peng,^{1,2} Chang,^{2,3} Ming-Ho Lin,¹ Wei-Su Chen,³
Frederick Chen,³ and Ming-Jinn Tsai^{3,*}

Address Format: Working Unit (Department), Institution, City, State, Post Code, Country

¹*Department of Materials Science and Engineering, National Tsing-Hua University, Hsinchu 300, Taiwan*

²*Institute of Photonics and Optoelectronics, National Taiwan University, Taipei 106, Taiwan*

³*Electronics and Optoelectronics Research Laboratory, Industrial Technology Research Institute, Chutung, Hsinchu 310, Taiwan*

***Corresponding author; Email:** [Provide correct email address here](#)

Document Type: [leave space here for Editor](#)

Submitted:**Date**..... **Accepted:****Date**.....

Abstract

The reversion of polarity within bipolar resistive switching operation occurs in Pt/HfO₂/TiN and Pt/Hf/HfO₂/TiN resistive random access memory devices. This reversion of voltage polarity is the result of interface generation which induces a conduction mechanism transformation from Poole-Frenkel emission to space charge limited current mechanism. To prove the reversion of polarity, this study uses curve fitting of I-V relations to verify the conduction mechanism theoretically and physical analysis to verify the oxygen ion distribution practically. The proposed Pt/Hf/HfO₂/TiN devices exhibit good resistive switching characteristics, such as good uniformity, low voltage operation, robust endurance (10³ dc sweep), and long retention (3×10⁴ s at 85 °C).

Keywords: HfO₂, Resistive random access memory, Hf Metal Layer, polarity reversal.

****First Time Use of Abbreviations:** No abbreviations are allowed in the title and abstract, therefore, all abbreviations should be defined the first time they are used within the title and text. For example, use first time as; Fourier transform infrared (FTIR) spectroscopy, scanning electron microscopy (SEM), transmission electron microscope (TEM), X-ray diffraction (XRD), X-ray photoelectron spectroscopy (XPS), Visible/near-infrared (Vis/NIR) spectroscopy, X-ray absorption fine structure (EXAFS) spectroscopy, etc.

1. Introduction

Resistive random access memory (RRAM) is an ideal candidate for non-volatile memory applications because of its simple structure, great scalability, fast switching speed, low power consumption, and compatibility with complementary metal-oxide semiconductor technology [1,2]. RRAM devices achieve the memory effect using the switchable resistance transformation between a high resistance state (HRS) and a low resistance state (LRS), and typically consist of a metal/insulator/metal structure. RRAM devices generally have two switching modes (unipolar and bipolar), which alternate based on the operating voltage polarity. Unipolar resistive switching occurs in any single voltage bias and does not depend on voltage polarity. Conversely, bipolar resistive switching depends on the variation of voltage polarity to complete the set (i.e., from the HRS to the LRS) and reset (i.e., from the LRS to the HRS) processes. Recent developments in RRAM have shifted to bipolar RRAM for several advantages, including a stable ON/OFF ratio, robust endurance, good retention, smaller switching voltage fluctuation, and the one selector-one resistor (1S1R) application [3]. The transition metal oxide, HfO_2 , is already widely used in semiconductor industries because of its superior physical properties, such as large permittivity, subsequent band gap, and excellent thermal stability [4]. In addition to its use as high-k/metal gate stacks, HfO_2 -based RRAM has attracted significant attention for its potential in next-generation nonvolatile memory. HfO_2 -based RRAM devices are formed by an electric-field induced conductive filaments formation/rupture process, and possess superior bipolar resistive switching for future RRAM applications.

The localized filamentary conducting paths in the thin films are diverse in each switching, leading to the nonuniform distributions of switching voltages and resistance states, which result in irresolvable errors in the RRAM operations. Thus, how to effectively improve the stability of switching behavior is an essential issue for practical application of the RRAM. Researchers have used many methods to improve resistive switching characteristics and change thin-film properties, such as embedding nanocrystals [5], doping effects [6,7], and embedding metal layer [8-11]. The embedding metal layer method typically serves as an interfacial oxygen storage layer, leading to oxygen ion concentration variation and diffusion. This in turn confines the conductive filament formation and rupturing within insulators and improves the uniformity of resistive switching characteristics. The interfacial layer also play a key role in polarity effect and resistive switching, and is dominant in the conversion of polarity from unipolar resistive switching to bipolar resistive switching, as shown by Yoo *et al.* [12] The reversion of polarity within bipolar resistive switching operation in Pt/ HfO_2 /TiN and Pt/Hf/ HfO_2 /TiN devices was observed in this work. The polarity reversion may be significantly affected by interfacial layer generation, inducing the change of conduction mechanisms in two device structures. The I-V relation and physical analysis in this study both provide proofs of the reversion of polarity. Pt/Hf/ HfO_2 /TiN RRAM

devices also exhibit good resistive switching characteristics by inserting Hf metal layer resulted in the production of HfO_x layer as an oxygen storage layer.

2. Experimental Details

In this study, RRAM devices consist of Pt/HfO₂/TiN and Pt/Hf/HfO₂/TiN structures. HfO₂ thin films were deposited on TiN (50 nm)/Ti (150 nm)/SiO₂ (200 nm)/p-Si substrates at 200 °C using the atomic layer deposition (ALD) method. The HfO₂ thin film (derived from TEMAH and H₂O precursors) was controlled at approximately 10 nm, and the deposition thickness of HfO₂ per ALD cycle was approximately 0.1 nm. After HfO₂ thin-film deposition, Hf and Pt metal layers measuring 40 nm and 70 nm in thickness were capped continuously by dc sputtering and patterned by a shadow mask with a diameter of 200 μm. The Pt capping layer prevents oxygen penetration from the atmosphere. The Pt/Hf/HfO₂/TiN device was subjected to post metal annealing (PMA) at 400 °C for 30 s in a N₂ atmosphere. For a comparison, a reference sample made without Hf layer and PMA process was also prepared, denoted as Pt/HfO₂/TiN device. The chemical-bonding states of Hf atoms in thin films were analyzed using the X-ray photoelectron emission spectrum (XPS). The electrical properties of the devices were measured using a Keithley 4200 semiconductor parameter analyzer. During the voltage-sweeping mode measurement, the bias was defined as positive when the current flowed from the top electrode to the bottom electrode, and was defined as negative when the current flowed in the opposite direction.

3. Results and Discussion

Figures 1a and 1b show the reverse polarity operation within bipolar resistive switching. Figure 1a shows that the set operation by a negative bias and the reset operation by a positive bias appear in the electrical characteristics of Pt/HfO₂/TiN RRAM devices. The same polarity was observed in similar devices described in previous researches [13,14]. After the Hf metal layer deposition and PMA processes, Pt/Hf/HfO₂/TiN RRAM devices show reverse polarity operation (i.e., the set operation by a positive bias, and the reset operation by a negative bias) in a stable resistive switching situation, as shown in Fig. 1b. The experimental results and literatures review in this study will confirm that the reverse polarity is correlated with interface-producing and conduction mechanism, transforming between two structures. In Pt/HfO₂/TiN RRAM devices, the conduction mechanism in pure HfO₂ thin films is usually attributed to the Poole-Frenkel emission [15,16]. The Poole-Frenkel emission equation can be expressed as

$$J = (qN_c\mu)E \exp \left[-\frac{q\Phi_t}{kT} + \frac{q\sqrt{qE/\pi\epsilon_\gamma\epsilon_0}}{r kT} \right]$$
, in which q is the electronic charge, N_c is the density of states in the conduction band, μ is the electronic drift mobility, $q\Phi_t$ is the trap level below the conduction band, ϵ_γ is the dynamic dielectric constant, ϵ_0 is the permittivity of free space, k is

Boltzmann's constant, T is the temperature, and r is a coefficient ranging between 1 and 2 [17,18]. If $r = 2$, the conduction mechanism is so-called the normal Poole-Frenkel emission. However, when the insulator contains another influential trap, r is equal to 1 and the conduction is called the modified Poole-Frenkel emission. In the reset process, the $\ln(J/E) - \sqrt{E}$ relationship of the HRS in the high electric field exhibits linear dependence, as shown in Fig. 2a. Accordingly, a refractive index of $n = 2.05$ can be obtained from the slope of the Poole-Frenkel plot at $r = 1$. This value is close to that of HfO_2 thin films reported in previous studies [19,20]. The consistency between these results and fitting data implies that Poole-Frenkel emission is the primary conduction mechanism in Pt/ HfO_2 /TiN RRAM devices.

Voltage polarity during resistive switching operation in the Pt/ HfO_2 /TiN RRAM device can be reversed by Hf metal deposition and the PMA process. This study applies theoretical deduction and physical analysis to investigate the reason for this polarity reversion. Initially, curve fitting was executed for the negative bias region of I-V characteristics in the Pt/Hf/ HfO_2 /TiN RRAM device. Figure 2b shows the resulting double-logarithmic plots. In the reset operation, Child's square law ($I \sim V^2$) is obeyed in the high-voltage bias by slope ~ 2 in the HRS, whereas Ohm's law ($I \sim V$) is obeyed in the low-voltage bias by slope ~ 1 in the HRS. According to the fitting results, the conduction mechanism of the proposed Pt/Hf/ HfO_2 /TiN RRAM devices is caused by space charge limited current (SCLC) mechanism [9,16,21]. Many studies have indicated that the SCLC mechanism is related to the insulating interfacial layer formation between metal layers and oxide thin films. This suggests the presence of an oxide interfacial layer between the Hf metal and the HfO_2 thin film, which might be partial oxide HfO_x ($x < 2$) [9,16,21]. After the PMA process, many oxygen ions may diffuse from the HfO_2 thin film to the Hf metal, resulting in the formation of HfO_x with oxygen deficiencies and Hf oxidation. To verify upon deductions of Pt/ HfO_2 /TiN and Pt/Hf/ HfO_2 /TiN RRAM devices, XPS analysis was adopted to characterize the distribution of oxygen. The XPS data, which were obtained at a fixed sputtering rate, shows localization near the interface. Figures 3a and 3b show the XPS spectra of the Hf 4f core levels of the pure HfO_2 thin film and the Hf/ HfO_2 structure. Figure 3a shows that the Hf 4f core level correlates with the pure HfO_2 thin film. However, the Hf 4f region in the Hf/ HfO_2 structure correlates with three spin-orbit doublets, each with corresponding $4f_{7/2}$ binding energies at 14.21, 15.4, and 18.26 eV [22]. The pink, green and red lines in this figure represent the Hf metal (Hf^0), the suboxide (HfO_x) and the fully oxidized hafnium (HfO_2) signals, respectively. These XPS results confirm the presence of an interfacial layer between the Hf metal and the HfO_2 thin film. Based on these results, the Pt/Hf/ HfO_2 /TiN RRAM device with an interfacial layer between the Hf layer and the HfO_2 thin film was dominated by the SCLC conduction mechanism. The polarity reversion of resistive switching behaviors can be explained by the effect of the interfacial layer, which fixes the oxygen diffusion region in the upper

interface. The Pt/HfO₂/TiN devices did not exhibit this phenomenon. Figure 4 shows the possible switching mechanism with different directions of applied bias. In virgin Pt/Hf/HfO₂/TiN devices after PMA (Fig. 4a), the oxygen storage layer getters oxygen ions and leaves charged oxygen vacancies in the oxide thin film, which makes the oxide thin film oxygen-deficient and conductive. Because the HfO₂ thin film becomes more conductive, a smaller-forming voltage (~1 V) can be applied to connect filaments formed by oxygen vacancies. When applying a positive bias to the top electrode (Fig. 4b), the external voltage enforces charged oxygen vacancies to form a conductive filament. This subsequently switches the device to the LRS. After applying a negative bias to the top electrode (Fig. 4c), the oxygen ions drift to the HfO₂ thin film from the interfacial layer and reoxidize the conductive filament, rupturing the filaments. This subsequently switches the device to the HRS. Figures 5a and 5b show a comparison of the uniformity parameters of the two devices based on cumulative probability statistics. The Pt/Hf/HfO₂/TiN RRAM devices exhibit more uniform resistive switching performance than Pt/HfO₂/TiN RRAM devices in both resistance and voltage distributions. The low operation voltages (lower than 1 V) in the Pt/Hf/HfO₂/TiN device, reveals the potential for low-power RRAM applications. The Pt/Hf/HfO₂/TiN devices also exhibit excellent resistive switching properties in both the endurance and retention test. After a 10³ dc sweep, the HRS and LRS maintain a stable resistance ratio higher than ten without decay, as shown in Fig. 6a. The dispersion of operation voltages demonstrates the high switching uniformity, as shown in Fig. 6b. Figure 6c shows their good data storage ability (3×10⁴ s) under 100 mV stress at 85 °C with nondestructive read-out.

4. Conclusions

In conclusion, this study shows that inserting a Hf metal layer into a Pt/HfO₂/TiN device and subjecting it to a PMA process creates a Pt/Hf/HfO₂/TiN device that exhibits polarity reversion in the resistive switching property. Inserting a Hf metal layer and performing the PMA process activated the Hf metal layer as an oxygen storage layer, which makes redox fixed near the interface between the Hf metal and the HfO₂ thin film. Consequently, the interface generation (HfO_x) that makes the conduction mechanism switch to SCLC mechanism from Poole-Frenkel emission, leading to a polarity reversion. The proposed Pt/Hf/HfO₂/TiN devices also exhibited good resistive switching characteristics and switching uniformity, with a low-voltage operation, 10³ dc sweep endurance, and 3×10⁴ s retention test at 85 °C.

Acknowledgments

References and Notes

Please use **HARVARD Referencing Style** from **Google Scholar** (<https://scholar.google.com>).

All references should be listed in a proper Harvard style on a separate page, numbered in the sequence in which they occur in the text. Cite references numerically in a **bracket [x]** in the text and follow the same numerical order in the "Reference List" at the end of the manuscript.

Do not use the phrases "et al." and "ibid." in the reference list, instead, include names of all authors.

Authors could directly **copy** references in a Harvard style from the Google Scholar (<https://scholar.google.com>) and then **paste** in the Reference List of the manuscript as such.

EXAMPLES

1. Journal Articles

Xu, Y., Bai, H., Lu, G., Li, C. and Shi, G., **2008**. Flexible graphene films via the filtration of water-soluble noncovalent functionalized graphene sheets. *Journal of the American Chemical Society*, 130(18), pp.5856-5857.

Kim, K.S., Kim, K.H., Nam, Y., Jeon, J., Yim, S., Singh, E., Lee, J.Y., Lee, S.J., Jung, Y.S., Yeom, G.Y. and Kim, D.W., **2017**. Atomic layer etching mechanism of MoS₂ for nanodevices. *ACS Applied Materials & Interfaces*, 9(13), pp.11967-11976.

2. Book

Nalwa, H.S. and Miyata, S., eds., **1996**. *Nonlinear Optics of Organic Molecules and Polymers*. Boca Raton, CRC Press.

3. Book Chapter

Krill, C.E., Harberkorn, R. and Birringer, R., **1999**. in *Handbook of Nanostructured Materials and Nanotechnology*, edited by H. S. Nalwa, Academic Press, Vol. 2, pp.155-211.

4. Website

National Renewable Energy Laboratory (NREL) (<https://www.nrel.gov/solar>)

5. Conference Proceedings

Kimura, J. and Shibasaki, H., eds., (**1995**). Recent Advances in Clinical Neurophysiology. *Proceedings of the 10th International Congress of EMG and Clinical Neurophysiology*, October 15-19; Kyoto, Japan. pp.10-15.

ALL FIGURES IN HIGH QUALITY REQUIRED

Important Note – Poor/blurred quality figures will not be accepted at all. There are *no charges* for color figures whatsoever so please make all figures in COLORS for a better presentation. It is very important to use **Large Fonts for Numbering and Ligands** in all figures as shown below.

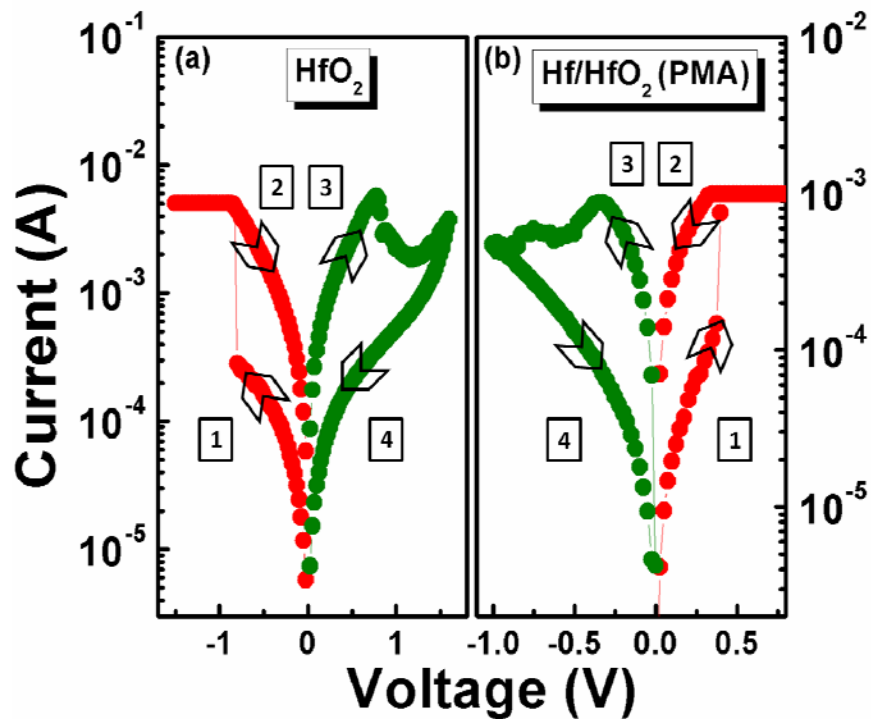


Figure 1. Reverse polarity operation in resistive switching between Pt/HfO₂/TiN and Pt/Hf/HfO₂/TiN devices.

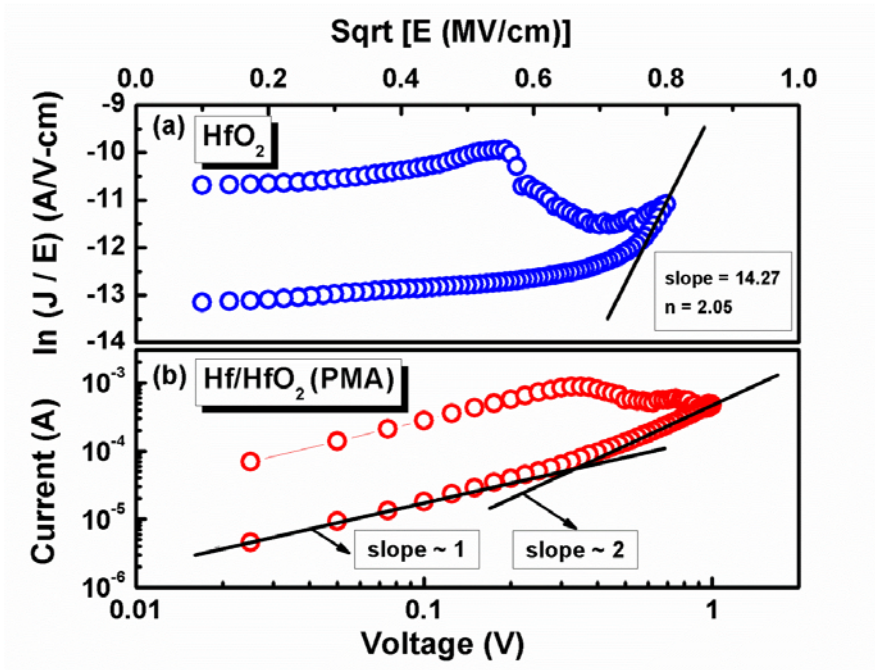


Figure 2. Curve fitting in Pt/HfO₂/TiN devices (a) Poole-Frenkel emission and in Pt/Hf/HfO₂/TiN devices (b) SCLC mechanism.

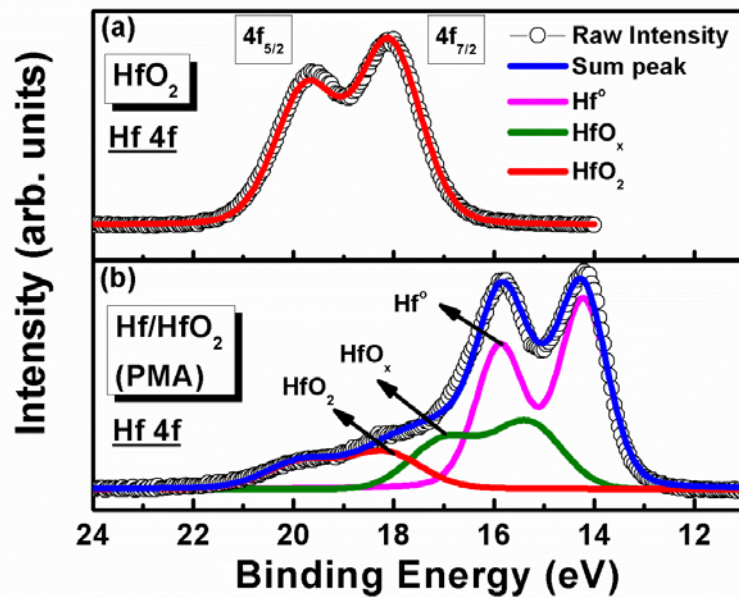


Figure 3. XPS spectra of Hf 4f core levels: (a) the HfO₂ thin film. (b) Interface between Hf/HfO₂.

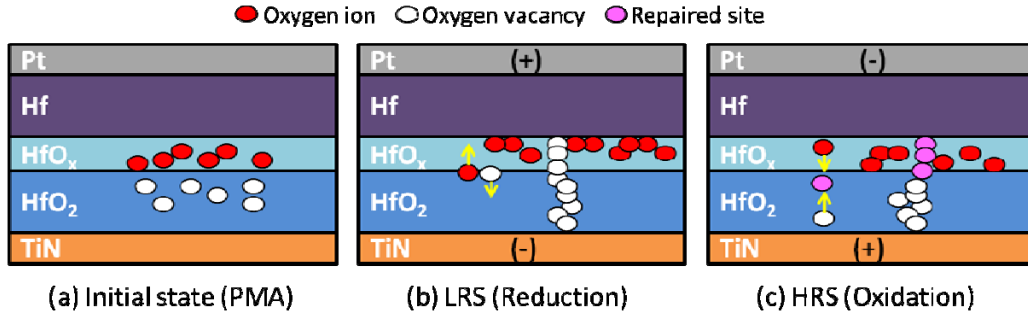


Figure 4. Possible scenarios of switching mechanisms for the Pt/Hf/HfO₂/TiN device with positive-bias or negative-bias voltage.

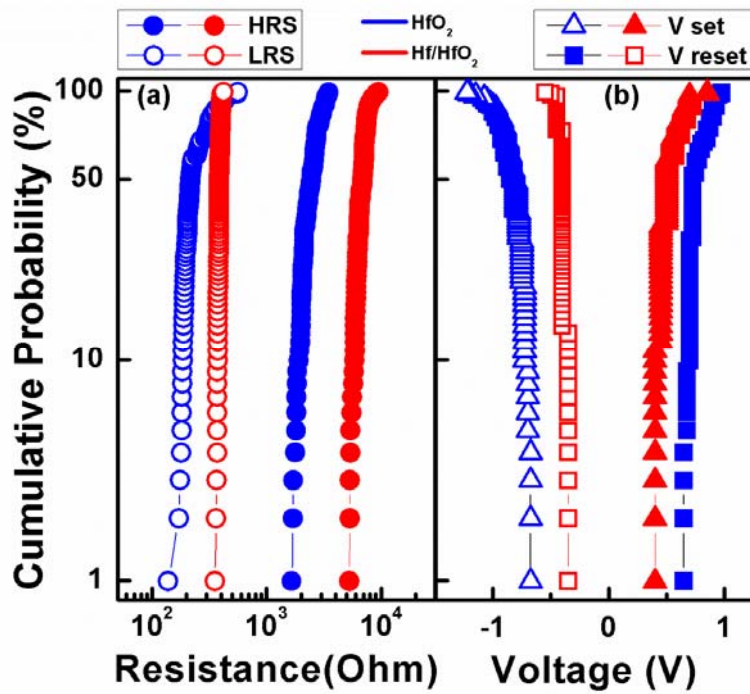


Figure 5. Statistical distribution of resistive switching parameters during 100 continuous cycles in both Pt/HfO₂/TiN and Pt/Hf/HfO₂/TiN devices. (a) HRS and LRS. (b) V_{set} and V_{reset}.

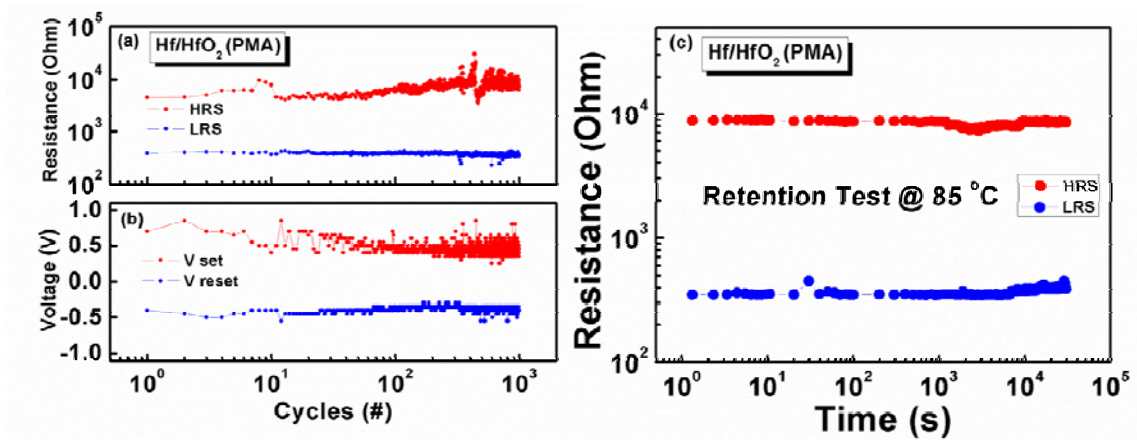


Figure 6. The 10³ stable endurance cycles of the Pt/Hf/HfO₂/TiN device: (a) HRS and LRS. (b) V_{set} and V_{reset}. (c) Data retention characteristics at 85 °C under 100mV stress.



Dynamic Characteristics Analysis on Coupled Vibration Models of Variable Gear Meshing in Forest Engineering Equipment Power Rear Transmission System

Author Name Format: Firs_Name Middle_Name Family_Name

Dacheng Pei¹, Xigui Wang^{2,*}, Xibin Dong^{2,*}, Yongmei Wang³, Yong Tang⁴, and Xue Zhou⁵

¹Aerospace School, Harbin Institute of Technology, Harbin 150001, PRC

²Engineering Technology School, Northeast Forestry University, Harbin 150040, PRC

³Motorcar Engineering School, Heilongjiang Institute of Technology, Harbin 150036, PRC

⁴Departments of Product Quality Management, Chongqing Gearbox Co., Ltd., Chongqing 402263, PRC

⁵Biology Teaching Group, No. 1 Middle School of Jiamusi City, Jiamusi 154000, PRC

In this paper, we take gear system as research object, and dynamic characteristics of gear pair meshing process as core, our purpose is to increase and improve dynamic performance of forest engineering equipment power rear transmission system (PRTS). Based on full consideration of this system components dynamic characteristics, used on theory and method of vibration mechanics, and studied on basic law of vibration, shock and noise in the process of transferring power and movement of forest engineering equipment PRTS. Example analysis results verification by using varied gear meshing coupled vibration model shows that gear pairs end surface meshing line direction relative to the dynamic response of vibration acceleration and RMS value of acceleration under working velocity, the vibration of the gear axial, and the load bearing transmitted to box body bearing hole inner wall. It provides theoretical basis for rear drive system design and manufacture with small vibration, low noise, high reliability and high transmission performance. The varied gear meshing coupled vibration model demonstrated in this paper may be applied for many military systems needed for the dynamic performance when a suitable gear meshing coupled vibration model is developed.

Keywords: Gear System, Dynamic Characteristics, Gear Meshing, Coupled Vibration Model, PRTS.

References should be listed in the REFERENCES section, and numbered in the sequence in which they occur in the text. Cite references numerically in a superscript in the text

1. INTRODUCTION

The dynamics main problem of forest engineering equipment PRTS is to determine its dynamic excitation. The key is to establish gear meshing coupling vibration model in analyzing forestry PRTS dynamics. Early gear dynamics model was single degree of freedom, which was mainly to determine gear teeth meshing dynamic load factor.¹⁻³ The gear lateral vibration displacement was not considered and the support was assumed to be rigid.⁴⁻⁶ the gear pair torsional vibration model was mainly studied in gear pairs dynamic meshing. Especially for dynamic excitation results, were very crucial for gear pair's torsional vibration, which played an important role in forestry PRTS stability.

The geared mechanical systems have been widely used in many industrial fields. Some examples include forest

engineering equipment power rear drive system, which are often supported by lubricated bearings.⁷⁻⁹ Thus, it is clear that an actual PRTS geared system may exhibit very complex coupling dynamic features. Due to the change of gear teeth meshing position, it causes to the change of gear teeth stiffness in the meshing process. The time-varying mesh stiffness produces dynamic meshing force, and applying a dynamic excitation for forest engineering equipment PRTS, which stability is affected, mainly caused by the factors of self-exciting vibration parameters.¹⁰⁻¹² Therefore, a correct and deep understanding of gear meshing coupled vibration model of forest engineering equipment PRTS is primordial importance to control the reliability and performance of the system, as well as to ensure the smooth and safe operating conditions.

In the field of highly diversified forest engineering equipment PRTS, the dynamics of gear meshing coupled vibration model with the considered meshing impact and

*Authors to whom correspondence should be addressed.

lubricated bearing stiffness has attracted much attention over the past few decades.¹³⁻¹⁵

Forest engineering equipment PRTS which is a complex structure system including gears pair, gear shafts, bearings and other components is one of the most important mechanical components in equipment.¹⁶⁻¹⁸ For this type of PRTS rotating structure, due to the role of PRTS rotation system with gear meshing, vibration characteristics and dynamic response may change rapidly.¹⁹⁻²¹ Recently, many attempts have been made to analyze dynamic characteristics of PRTS, and some remarkable achievements have been achieved.²² The research content involves the dynamics modeling of PRTS, the inherent characteristics of PRTS, the dynamic response analysis for solving PRTS' vibration, and the vibration and noise suppression of forest engineering equipment PRTS.

We have established 3 gear meshing coupling dynamic models of forest engineering equipment PRTS. On this basis, the dynamic responses of forestry PRTS have been studied. Furthermore, we have verified by examples with varied gear meshing coupled vibration model in accordance with forestry specific actual conditions. The verification results contribute to the study of forest engineering equipment PRTS vibration damage decrease.

2. THE THEORETICAL MODEL OF FORESTRY PRTS

2.1. Spur Gear Vibration Model of Meshing Type Bending Torsion Axial Coupling

The structure diagrammatic sketch of spur gear vibration model (SGVM) of meshing type bending torsion axial coupling is shown in Figure 1. In order to make the analysis without a loss of the generality, the forestry PRTS is a three-dimensional space vibration system. Due to simplify

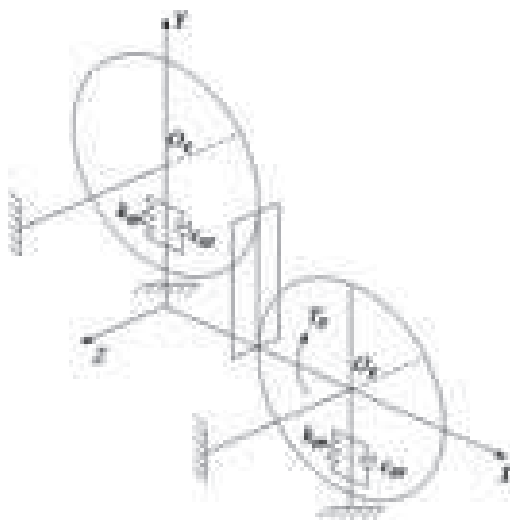


Fig. 1. SGVM of meshing type bending torsion axial coupling.

the forestry PRTS, the 4 DoFs system without considering the friction caused by relative sliding between meshing gear teeth surfaces is proposed.

As shown in Figure 1, k_{gy} and k_{py} are the forestry PRTS' equivalent bearing stiffness of gear pairs, c_{gy} and c_{py} are the forestry PRTS' equivalent bearing damping of gear pairs, T_p is the input torque, β is the angle between the direction of the first line and a horizontal center of gear pairs. Then, according to the law of Newtonian mechanics, the dynamic equation of the forestry PRTS can be expressed as

$$\begin{cases} m_p \ddot{y}_p + c_{py} \dot{y}_p + k_{py} y_p = -F_y \\ I_p \ddot{\theta}_p = -F_y \cdot R_p + T_p \end{cases} \quad (1)$$

$$\begin{cases} m_g \ddot{y}_g + c_{gy} \dot{y}_g + k_{gy} y_g = F_y \\ I_g \ddot{\theta}_g = F_y \cdot R_g - T_g \end{cases} \quad (2)$$

Where for $i = p, g$, y_i is the level shift vibration displacement of the gear center point in the y direction, θ_i is the angular vibration displacement of the gear center point along the y direction, F_i is the meshing force of gear pairs along the meshing line, R_i is the gear's radius. In order to eliminate the rigid body displacement, we have assumed that $q = R_p \theta_p - R_g \theta_g$ is trustworthy, therefore the forestry PRTS' differential equations of motion are obtained.

$$\begin{cases} m_p \ddot{y}_p + c_{py} \dot{y}_p + k_{py} y_p + c_m (\dot{y}_p - \dot{y}_g + \dot{q}) \\ \quad + k_m (y_p - y_g + q) = F_p + F_g \\ m_g \ddot{y}_g + c_{gy} \dot{y}_g + k_{gy} y_g + c_m (\dot{y}_g - \dot{y}_p - \dot{q}) \\ \quad + k_m (y_g - y_p - q) = -F_p - F_g \\ m \ddot{q} + c_m \dot{q} + k_m q + c_m (\dot{y}_p - \dot{y}_g) \\ \quad + k_m (y_p - y_g) = T_p/R_p + (F_p + F_g) \end{cases} \quad (3)$$

Where for $i = 1, 2$, m_i is the mass of the gear shaft, $m_i = I_i/R_i^2$; $m = m_1 m_2 / (m_1 + m_2)$, and I_i is the rotational inertia of the gear shaft.

2.2. Helical Gear Vibration Model of Meshing Type Bending Torsion Axial Coupling

The structure diagrammatic sketch of helical gear vibration model (HGVM) of meshing type bending torsion axial coupling is shown in Figure 2. Considering the axial dynamic meshing force when helical gear meshing will be produced, the forestry PRTS is a three-dimensional space vibration system. Further simplified the forestry PRTS, the 6 DoFs system without considering the friction caused by relative sliding between teeth surfaces is shown.

As illustrated in Figure 2, k_{gy} , k_{py} , k_{gz} and k_{pz} are the forestry PRTS' equivalent bearing stiffness of gear pairs, c_{gy} , c_{py} , c_{gz} and c_{pz} are the forestry PRTS' equivalent bearing damping of gear pairs, T_p is the input torque, β is the

Label each figure and refer it in the context

angle between the direction of the first line and a horizontal center of gear pairs. Then, according to the law of Newtonian mechanics, the dynamic equation of forestry PRTS can be expressed as

$$\begin{cases} m_p \ddot{y}_p + c_{py} \dot{y}_p + k_{py} y_p = -F_y \\ m_p \ddot{z}_p + c_{pz} \dot{z}_p + k_{pz} z_p = -F_z \\ I_p \ddot{\theta}_p = -F_y \cdot R_p + T_p \end{cases} \quad (4)$$

$$\begin{cases} m_g \ddot{y}_g + c_{gy} \dot{y}_g + k_{gy} y_g = F_y \\ m_g \ddot{z}_g + c_{gz} \dot{z}_g + k_{gz} z_g = F_z \\ I_g \ddot{\theta}_g = F_y \cdot R_g - T_g \end{cases} \quad (5)$$

Where for $i = p, g$, y_i and z_i are the level shift vibration displacement of the gear center point in the y and z direction, respectively, θ_i is the angular vibration displacement of the gear center point along the y and z direction, F_i is the meshing force of gear pairs along the meshing line, R_i is the gear's radius. In order to eliminate the rigid body displacement, the formula $q = R_p \theta_p - R_g \theta_g$ is assumed to be true. Therefore, the forestry PRTS' differential equations of motion are proposed.

$$\begin{cases} m_p \ddot{y}_p + c_{py} \dot{y}_p + k_{py} y_p + \cos \beta c_m (\dot{y}_p - \dot{y}_g + \dot{q}) \\ \quad + \cos \beta k_m (y_p - y_g + q) = F_y + F_z \\ m_p \ddot{z}_p + c_{pz} \dot{z}_p + k_{pz} z_p + \sin \beta c_m \tan \beta (\dot{y}_p - \dot{y}_g + \dot{q}) \\ \quad + \sin \beta c_m (\dot{z}_p - \dot{z}_g) + \sin \beta k_m \tan \beta (y_p - y_g + q) \\ \quad + \sin \beta k_m (z_p - z_g) = \tan \beta (F_y + F_z) \\ m_g \ddot{y}_g + c_{gy} \dot{y}_g + k_{gy} y_g + \cos \beta c_m (\dot{y}_g - \dot{y}_p - \dot{q}) \\ \quad + \cos \beta k_m (y_g - y_p - q) = -F_y - F_z \\ m_g \ddot{z}_g + c_{gz} \dot{z}_g + k_{gz} z_g - \sin \beta c_m \tan \beta (\dot{y}_p - \dot{y}_g + \dot{q}) \\ \quad + \sin \beta c_m (\dot{z}_g - \dot{z}_p) - \sin \beta k_m \tan \beta (y_p - y_g + q) \\ \quad + \sin \beta k_m (z_g - z_p) = -\tan \beta (F_y + F_z) \\ m \ddot{q} + c_m \cos \beta \dot{q} + k_m \cos \beta q + c_m \cos \beta (\dot{y}_p - \dot{y}_g) \\ \quad + k_m \cos \beta (y_p - y_g) = T_p / R_p + (F_y + F_z) \end{cases} \quad (6)$$

Where for $i = 1, 2$, m_i is the mass of the gear shaft, $m_i = I_i / R_i^2$, $m = m_1 m_2 / m_1 + m_2$, and I_i is the rotational inertia of the gear shaft.

2.3. Herringbone Gear Vibration Model of Meshing Type Bending Torsion Axial Coupling

Forestry PRTS mainly adopts herringbone gears, so the thrust bearing of gear shaft does not bear the axial load, it only has a positioning function. For forest engineering practical application, herringbone gears of forestry PRTS must be one gear axially floating, in order to balance the axial force which generated by axial float. In general, the small gear of forestry PRTS is an axial float. When considering the axial deformation of gear shaft with bearing

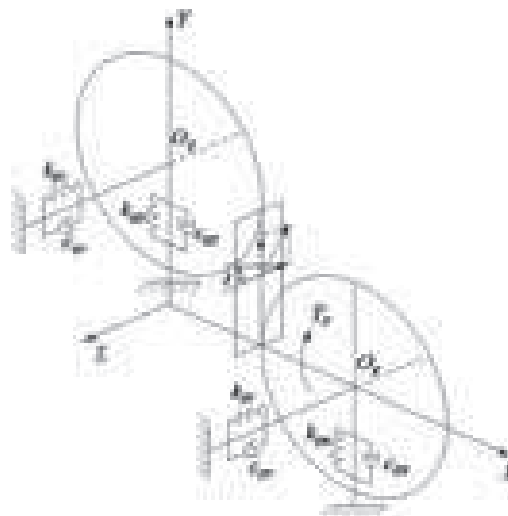


Fig. 2. HGVM of meshing type bending torsion axial coupling.

bending torsion, the structure diagrammatic sketch of herringbone gear vibration model (BGVM) of meshing type bending torsion axial coupling is shown in Figure 3. Due to simplify PRTS, the 12 DoFs system without considering the friction caused by relative sliding between teeth surfaces is studied in the paper.

As shown in Figure 3, where for $i = p, g$, $j = 1, 2$, y_{ij} and z_{ij} are the level shift vibration displacement of the gear center points O_{p1} , O_{p2} , O_{g1} and O_{g2} in the y and z direction, respectively, R_i is the gear's radius. Where for $i = 1, j = 2$, θ_{ij} is the angular vibration displacement of the gear center point along the y and z direction, respectively, $k_{g_{iy}}$, $k_{p_{iy}}$, $k_{g_{jy}}$ and $k_{p_{jy}}$ are the forestry PRTS' equivalent bearing stiffness in O_{p1} , O_{p2} , O_{g1} and O_{g2} points of gear pairs, respectively, $k_{g_{iz}}$, $k_{g_{jz}}$, $k_{g_{ijz}}$ and $k_{p_{ijz}}$ are the forestry

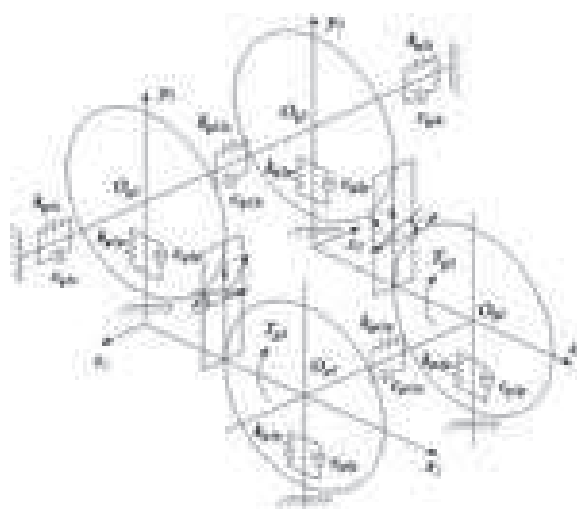


Fig. 3. BGVM of meshing type bending torsion axial coupling.

Table 1. The parameters of spur gear pairs.

Gear geometric parameter	Pinion gear	Large gear
Modulus (mm)	6	6
Teeth number	19	48
Teeth width (mm)	75	75
Shaft length (mm)	200	200
Shaft radius (mm)	45	55
pressure angle (°)	20	20
Quality (kg)	7.5	38.6
Moment of inertia [kg · m ²]	0.016	0.35
Density [g/cm ³]		7.85
Damping ratio coefficient (ξ)		0.10

PRTS' axial equivalent translational vibration stiffnesses of gear pairs, respectively, c_{giy} , c_{piy} , $c_{g jy}$ and $c_{p jy}$ are the forestry PRTS' equivalent bearing damping in O_{p1} , O_{p2} , O_{g1} and O_{g2} points of gear pairs, respectively, $c_{g iz}$, $c_{g jz}$, $c_{g iz}$ and $c_{p iz}$ are the forestry PRTS' axial equivalent translational vibration dampings of gear pairs, respectively, T_{p1} and T_{p2} are the input torque and the load torque, respectively, β is the angle between the direction of the first line and a horizontal center of gear pairs. Then, according to the law of Newtonian mechanics, the dynamic equation of the forestry PRTS can be expressed as

$$\begin{cases} m_p \ddot{y}_{p1} + c_{p1y} \dot{y}_{p1} + k_{p1y} y_{p1} = -F_{y1} \\ m_p \ddot{z}_{p1} + c_{p12z} (\dot{z}_{p1} - \dot{z}_{p2}) + k_{p12z} (z_{p1} - z_{p2}) = -F_{z1} \\ I_p \ddot{\theta}_{p1} = -F_{y1} \cdot R_p + T_{p1} \end{cases} \quad (7)$$

$$\begin{cases} m_g \ddot{y}_{g1} + c_{g1y} \dot{y}_{g1} + k_{g1y} y_{g1} = F_{y1} \\ m_g \ddot{z}_{g1} + c_{g12z} \dot{z}_{g1} + k_{g12z} z_{g1} + c_{g12z} (\dot{z}_{g1} - \dot{z}_{g2}) \\ + k_{g12z} (z_{g1} - z_{g2}) = F_{z1} \\ I_g \ddot{\theta}_{g1} = F_{y1} \cdot R_g - T_{g1} \end{cases} \quad (8)$$

$$\begin{cases} m_p \ddot{y}_{p2} + c_{p2y} \dot{y}_{p2} + k_{p2y} y_{p2} = -F_{y2} \\ m_p \ddot{z}_{p2} - c_{p12z} (\dot{z}_{p1} - \dot{z}_{p2}) - k_{p12z} (z_{p1} - z_{p2}) = -F_{z2} \\ I_p \ddot{\theta}_{p2} = -F_{y2} \cdot R_p + T_{p2} \end{cases} \quad (9)$$

$$\begin{cases} m_g \ddot{y}_{g2} + c_{g2y} \dot{y}_{g2} + k_{g2y} y_{g2} = F_{y2} \\ m_g \ddot{z}_{g2} + c_{g2z} \dot{z}_{g2} + k_{g2z} z_{g2} - c_{g12z} (\dot{z}_{g1} - \dot{z}_{g2}) \\ - k_{g12z} (z_{g1} - z_{g2}) = F_{z2} \\ I_g \ddot{\theta}_{g2} = F_{y2} \cdot R_g - T_{g2} \end{cases} \quad (10)$$

Where for $i = 1, 2$, m_i is the mass of the gear shaft, $m_i = I_i/R_i^2$, $m = m_1 m_2 / (m_1 + m_2)$, and I_i is the rotational inertia of the gear shaft.

3. EXAMPLE VERIFICATION AND ANALYSIS ON DIFFERENT WORKING CONDITIONS

3.1. Dynamic Analysis of Spur Gear Meshing Type Bending Torsional Coupled Vibration Model

For the example in this section, the rolling bearings support are adopted, other parameters are shown in **Table I**. Under stable condition, the load torque of the involute spur gear is 800 Nm, and the input velocity of the driving wheel is 2000 r/min. According to the initial parameters of spur gear, first the stiffness excitation curve and meshing impact force curve are fitted. Then, the stiffness excitation function and the meshing impact force excitation function are expanded into Fourier series. In the dynamic equation, the acceleration responses of the forestry PRTS are solved. Finally, the dynamic response results of the PRTS are obtained by the superposition principle. Based on this way, comprehensive meshing stiffness is shown in

Figure 4. Vibration acceleration of small gear support bearing is shown in Figure 5. Vibration acceleration of large gear support bearing is shown in Figure 6.

As illustrated in Figure 5, under stable condition of forestry PRTS, the maximum instantaneous acceleration is 41.2 m/s², and the RMS value of acceleration is 8.98 m/s², which is equivalent to the small gear support bearing.

As described in Figure 6, under stable condition of forestry PRTS, the maximum instantaneous acceleration is -5.32 m/s², and the RMS value of acceleration is 2.08 m/s², which is equivalent to the large gear support bearing.

3.2. Dynamic Analysis of Helical Gear Meshing Type Bending Torsional Coupled Vibration Model

In this example, the rolling bearings support are adopted, other parameters are shown in Table II. Under stable



Fig. 4. Comprehensive meshing stiffness.



Fig. 5. Vibration acceleration of small gear support bearing.

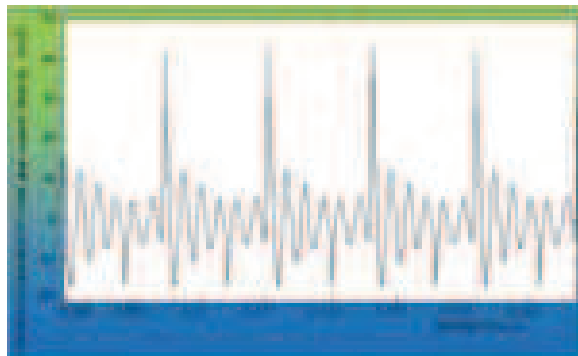


Fig. 6. Vibration acceleration of large gear support bearing.

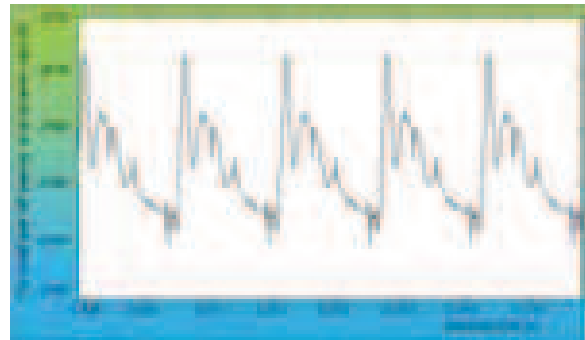


Fig. 8. The small gear left bearing hole inner wall axial dynamic load.

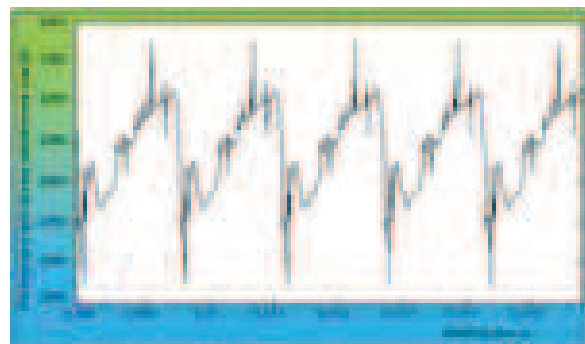


Fig. 9. The large gear right bearing hole inner wall radial dynamic load.

Table II. The parameters of helical gear pairs.

Gear geometric parameter	Pinion gear	Large gear
Normal modulus m_n (mm)	8	8
Teeth number	19	47
Teeth width (mm)	75	75
Shaft length (mm)	200	200
Shaft radius (mm)	45	55
pressure angle ($^\circ$)	20	20
Helix angle ($^\circ$)	9.92	9.92
Quality (kg)	7.8	40.2
Moment of inertia [$\text{kg} \cdot \text{m}^2$]	0.018	0.387
Density [g/cm^3]		7.85
Damping ratio coefficient (ξ)		0.10

condition, the load torque of the involute helical gear is 800 Nm, and the input velocity of the driving wheel is 2000 r/min. The research methods are the same as the spur gear model, the small gear left side gearbox bearing hole inner wall radial dynamic load is shown in Figure 7. The small gear left side gearbox bearing hole inner wall axial dynamic load is illustrated in Figure 8. The large gear right side gearbox bearing hole inner wall radial dynamic load is described in Figure 9.

The large gear right side gearbox bearing hole inner wall axial dynamic load is outlined in Figure 10.

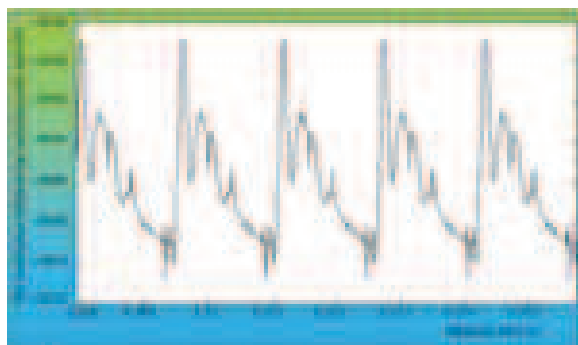


Fig. 7. The small gear left bearing hole inner wall radial dynamic load.

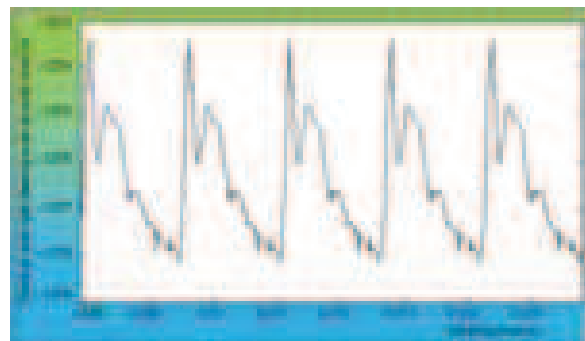


Fig. 10. The large gear right bearing hole inner wall axial dynamic load.

As shown in Figures 7 and 8, Under the stable condition of the forestry PRTS, the maximum values instantaneous acceleration where the gears bearing equivalent support are 9.56 m/s^2 (small gear) and 0.92 m/s^2 (large gear), the RMS acceleration are 2.06 m/s^2 (small gear) and 0.46 m/s^2 (large gear). It is near where the natural frequencies of PRTS, the maximum values of vibration amplitude component are 1.95 m/s^2 (small gear) and 0.43 m/s^2 (large gear). The FFT spectrum was not given.

As shown in Figures 9 and 10, the maximum values instantaneous acceleration where the gears bearing

Table III. The parameters of herringbone gear pairs.

Gear geometric parameter	Pinion gear	Large gear
Normal modulus m_n (mm)	8	8
Teeth number	17	44
Teeth width (mm)	168	168
Shaft length (mm)	300	300
Shaft radius (mm)	45	55
Pressure angle (°)	20	20
Helix angle (°)	24.45	24.45
Quality (kg)	17.8	101.2
Moment of inertia [$\text{kg} \cdot \text{m}^2$]	0.0157	0.586
Density [g/cm^3]		7.85
Damping ratio coefficient (ξ)		0.10

equivalent support are 5.68 m/s^2 (large gear) and 1.36 m/s^2 (small gear), the RMS acceleration are 2.96 m/s^2 (large gear) and 0.38 m/s^2 (small gear). It is near where the natural frequencies of the forestry PRTS, the maximum values of vibration amplitude component are 3.02 m/s^2 (large gear) and 0.41 m/s^2 (small gear). Therefore, the forestry PRTS should not have been in this frequency segment for a long time, so as to avoid resonance.

3.3. Dynamic Analysis of Herringbone Gear Meshing Type Bending Torsional Coupled Vibration Model

The discussion on herringbone gears of the forestry PRTS some characterized dynamic analysis conclusions similar to helical gears. The parameters of herringbone gears are shown in Table III. The small gear left bearing hole inner wall radial dynamic load, as shown in Figure 11. The large gear left bearing hole inner wall radial dynamic load, as shown in Figure 12.

As shown in Figures 11 and 12, the maximum values instantaneous acceleration where the gears bearing equivalent support are 61.57 m/s^2 (small gear) and 28.16 m/s^2 (large gear), the RMS acceleration are 8.14 m/s^2 (small gear) and 0.86 m/s^2 (large gear). It is near where the natural frequencies of the forestry PRTS, the maximum values of vibration amplitude component are 7.96 m/s^2 (small gear) and 0.83 m/s^2 (large gear). The FFT spectrum was not given.

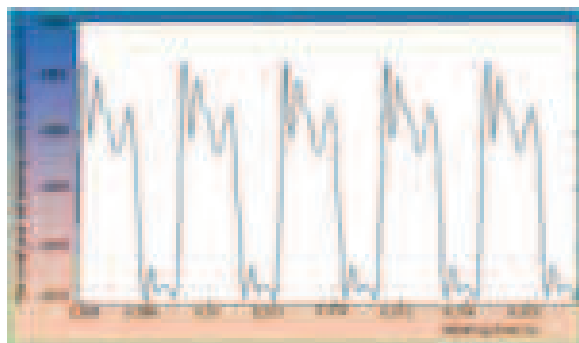


Fig. 11. The small gear left bearing hole inner wall radial dynamic load.

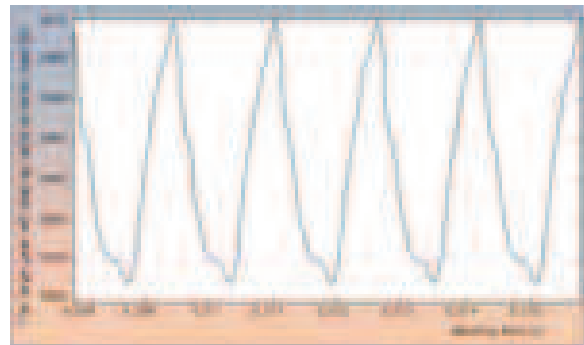


Fig. 12. The large gear left bearing hole inner wall radial dynamic load.

4. GEAR TEETH BENDING STRESS AND CONTACT STRESS CALCULATION PROCESS UNDER DYNAMIC CONDITIONS

There are usually material mechanics approximation method and dynamic finite element software modeling method to solve for gear teeth surface contact stress and teeth root bending stress. However, these calculation methods are basically unable to better reflect its dynamic characteristics in the complex forestry power rear drive system. In this paper, the loaded teeth contact analysis (LTCA) program in accordance with forestry PRTS actual conditions has been self-developed and used to calculate the stress value σ_{ei} which the unit load on teeth root bending stress checking points (where selected passive wheel tension side root midpoints as the test points), and to solve the gear teeth surface contact stress and gear teeth root bending stress by the Eqs. (11) and (12) under dynamic loading.

$$\sigma_{vhi} = \sqrt[2/3]{F_{vi}} \cdot \sigma_{ehi} \dots (i = 1 \dots n) \tag{11}$$

$$\sigma_{vbi} = F_{vi} \cdot \sigma_{ebi} \dots (i = 1 \dots n) \tag{12}$$

Refer equation in the text

Where for $i = 1 \dots n$, σ_{vi} is the gear root midpoint contact stress of meshing contact line, F_{vi} is the single teeth dynamic load of meshing contact line, n is the meshing teeth pair.

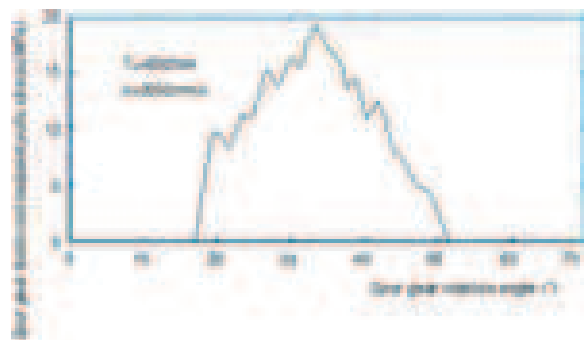


Fig. 13. Spur gear teeth root midpoint pulls stress.

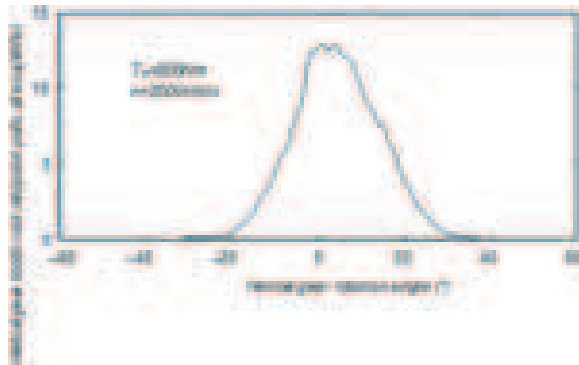


Fig. 14. Helical gear teeth root midpoint pulls stress.

In order to ensure the calculation accuracy and efficiency to reflect the actual changes fluctuation trend of gear teeth dynamic stress. F_{vi} is a critical parameter of the simulation numerical calculation. In the process of simulation numerical calculation and analysis, the gear teeth dynamic load calculated by the forestry PRTS dynamics model is divided into five equal parts according to the minimum and maximum value. The load distribution coefficients of each contact line under five loads are calculated by the LTCA program, the relation curves between load distribution coefficient and load size of any contact line are solved, and the dynamic loads of single teeth when gear meshing any moment are obtained.

In the given rotation velocity 2000 r/min and load torque 800 Nm condition, the dynamic stress change process of spur gear teeth root point pull side is shown as Figure 13. The dynamic stress change process of helical gear teeth root point pull side is shown as Figure 14. The dynamic stress change process of herringbone gear teeth root point pull sides are shown as Figures 15 and 16.

The complexity of the models for describing forestry PRTS and to predict their vibrational response under various conditions has always relied heavily on the available experience and traditional methods.

Although gear meshing coupled vibration of forestry PRTS has been identified and researched over many years,

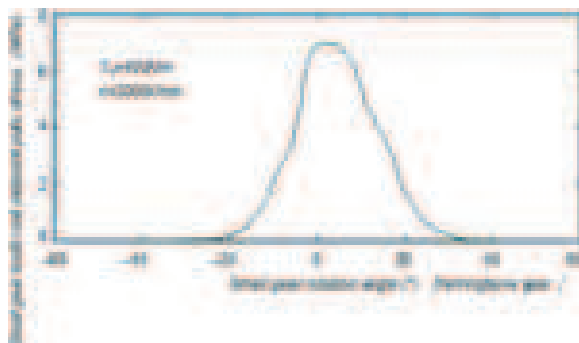


Fig. 15. Herringbone gear teeth root midpoint pulls stress (small gear).

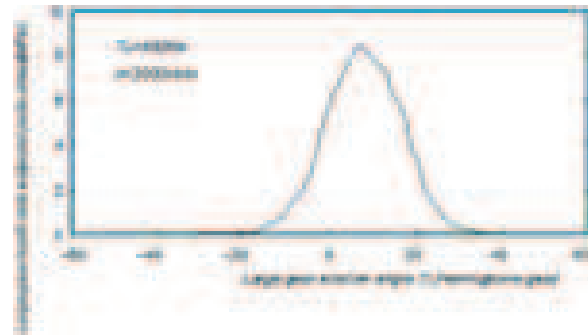


Fig. 16. Herringbone gear teeth root midpoint pulls stress (large gear).

the accuracy of conventional models for the calculation of coupled vibration response remains unacceptable in some cases. Improved models need to be developed notably for meshing resonance where loaded gears may be affected. It has been concluded that the vibration response of forestry PRTS structures may be poorly modelled by conventional modelling techniques and by uncoupling the gear pair's dynamic analyses.

5. CONCLUSIONS

In this study, the varied gear meshing coupled vibration model can be successfully conducted using forest engineering equipment power rear drive system (PRTS). The characterization of PRTS is essential to determine its coupled vibration response and the possible effects of such a response on forestry PRTS operations. The activation of gear pair meshing causes an excitation in resonance frequencies. This requires dynamic analysis to ensure that all relevant aspects affecting resonance behavior are captured. The gear meshing coupled vibration model is affected by input torque and rotational velocity. Torsional frequencies are also affected by the transmission shaft meshing stiffness as well as impact forces. It is concluded that PRTS vibration dynamic loads where gear meshing points are distributed to both ends of the bearing inner ring through the transmission shaft and then are delivered to the bearing hole inner wall of the gearbox body.

Dynamic analysis of varied gear meshing coupled vibration model of forestry PRTS in this study are useful, depending on the required accuracy, and the available information and resources. In cases where a high level of accuracy is required, the loaded teeth contact analysis (LTCA) program in accordance with forestry PRTS actual conditions has been self-developed and used to calculate the stress value.

Acknowledgment: The authors gratefully acknowledge support from the Northeast Forestry University (NEFU) as well as the Heilongjiang Institute of Technology (HLJIT). This work is supported by the Special Scientific Research Funds for Forest Non-profit Industry (Grant No. 201504508) and the Youth Science

References

1. Ma, S.-Y., Shen, C.-F. and Chen, L.-G., **2001**. An Efficient Motion Estimation Algorithm for Real-Time MPEG-4 Video Encoding on Multimedia Processors. *Proceedings of Workshop and Exhibition on MPEG-4*, June 20; San Jose, CA, USA. pp.67–70.
2. Abdou Khadre Diop, Tall, K., Farssi, S.M. and Diop, I., **2014**. Performances of the Estimation and Motion Compensation for the Reconstruction of Motion Areas in a Sequence Video Motion JPEG 2000. *International Conference on Advanced Communication Technology*, February 16–19; Pyeongchang, South Korea. pp.92–95.
3. Kuhn, P., **1999**. *Complexity Analysis and VLSI Architectures for MPEG-4 Motion Estimation*. Springer US, pp.93–106.
4. Li, R., Zeng, B. and Liou, M.L., **1994**. Newthree-step search algorithm for blockmotion estimation. *IEEE Transactions on Circuits and Systems for Video Technology*, 4(4), pp.438–442.
5. Po, L.-M. and Ma, W.-C., **1996**. A novel four-step search algorithm for fast blockmotion estimation. *IEEE Transactions on Circuits and Systems for Video Technology*, 6(3), pp.313–317.
6. Zhu, S. and Ma, K.-K., **2000**. A new diamond search algorithm for fast block-matching motion estimation. *IEEE Transactions on Image Processing*, 9(2), pp.287–290.
7. Zhu, C., Lin, X. and Chau, L.-P., **2002**. Hexagon-based search pattern for fast blockmotion estimation. *IEEE Transactions on Circuits and Systems for Video Technology*, 12(5), pp.349–355.
8. Lim, Y.-C., Min, K.-Y. and Chong, J.-W., **2003**. A Pentagonal Fast Block Matching Algorithm for Motion Estimation Using Adaptive Search Range. *Proceedings of IEEE International Conference on Acoustics, Speech, and Signal Processing*, April 6–10; Hong Kong, China. pp.669–672.
9. Palaniraj, P. and Sakhivel, G., **2018**. *Hexagonal Intersection-Based Inner Search to Accelerate Motion Estimation*, Lecture Notes in Electrical Engineering, Vol. 500, pp.375–381.
10. Pham, D.T., Otri, S., Ghanbarzadeh, A. and Kog, E., **2006**. Application of the Bees Algorithm to the Training of Learning Vector Quantisation Networks for Control Chart Pattern Recognition. *International Conference on Information & Communication Technologies*, April 24–28; Damascus, Syria. pp.1624–1629.
11. Pham, D.T., Otri, S., Afify, A., Mahmuddin, M. and Al-Jabbouli, H., **2007**. Data Clustering Using the Bees Algorithm. *40th CIRP International Manufacturing Systems Seminar*, University of Birmingham.
12. Po, L.-M., Ting, C.-W., Wong, K.-M. and Ng, K.-H., **2007**. Novel Point-Oriented Inner Searches for Fast Block Motion Estimation. *IEEE Transactions on Multimedia*, 9(1), pp.9–15.
13. Cuevasa, E., Zaldívar, D., Pérez-Cisnerosa, M., Sossab, H. and Osunab, V., **2013**. Block matching algorithm for motion estimation based on artificial bee colony (ABC). *Applied Soft Computing*, 13(6), pp.3047–3059.
14. Koc, E., **2010**. *The Bees Algorithm Theory, Improvements and Applications*, Ph.D. Thesis, Cardiff University, Cardiff, UK.
15. Kung, A.-M., Cheng, W.-S. and Jeng, J.-H., **2014**. *The Scientific World Journal*, 14, pp.11–12.
16. Du, G.-Y., Huang, T.-S., Song, L.-X. and Zhao, B.-J., **2005**. A Novel Fast Motion Estimation Method Based on Particle Swarm Optimization. *Proceedings of International Conference on Machine Learning and Cybernetics*, August 18–21; Guangzhou, China. pp.5032–5042.
17. Palaniraj, P. and Sakhivel, G., **2018**. Hybrid motion estimation algorithm based on PSO with dynamic threshold on static block detection. *Procedia Computer Science*, 132, pp.1487–1496.

References should be listed and numbered in the sequence in which they occur in the text.

Received: 30 October 2018. Accepted: 31 October 2018.